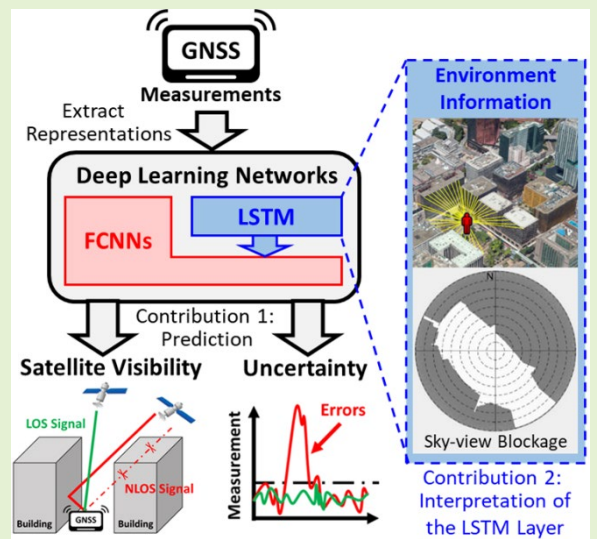


# Prediction on the Urban GNSS Measurement Uncertainty based on Deep Learning Networks with Long Short-Term Memory

Guohao Zhang, *Student Member, IEEE*, Penghui Xu, Haosheng Xu and Li-Ta Hsu, *Member, IEEE*

**Abstract**—The GNSS performance could be significantly degraded by the interferences in an urban canyon, such as the blockage of the direct signal and the measurement error due to reflected signals. Such interferences can hardly be predicted by statistical or physical models, making urban GNSS positioning unable to achieve satisfactory accuracy. The deep learning networks, specializing in extracting abstract representations from data, may learn the representation about the GNSS measurement quality from existing measurements, which can be employed to predict the interferences in an urban area. In this study, we proposed a deep learning network architecture combining the conventional fully connected neural networks (FCNNs) and the long short-term memory (LSTM) networks, to predict the GNSS satellite visibility and pseudorange error based on GNSS measurement-level data. The performance of the proposed deep learning networks is evaluated by real experimental data in an urban area. It can predict the satellite visibility with 80.1% accuracy and predict the pseudorange errors with an average difference of 4.9 meters to the labeled errors. Experiments are conducted to investigate what representations have been learned from data by the proposed deep learning networks. Analysis results show that the LSTM layer within the proposed networks may contain representations about the environment, which affects the prediction behavior and can associate with the real environment information.

**Index Terms**—deep learning, GNSS, LSTM, multipath, navigation, urban canyon



## I. Introduction

VARIOUS applications nowadays rely on accurate and reliable navigation solutions, such as intelligent transportation system (ITS) and location-based service (LBS) [1]. The global navigation satellite system (GNSS) is the most widely employed approach among different positioning techniques. The GNSS can directly provide a global positioning solution instead of a relative position estimation for the user, while maintaining an economical cost. However, the quality of the GNSS measurements can be easily degraded by the interferences related to the environment, introducing enormous errors during positioning [2].

Unlike the interference from atmospheric delays or satellite orbit bias, the modelling of the GNSS multipath error closely related to the environment surrounding the user is always a challenge, neither through a physical nor a statistical approach,

especially for an urban environment with complicated building structures [3]. The GNSS receiver may receive the reflected signal from the building surface in addition to the direct line-of-sight (LOS) signal, or even worst, the reflection alone, namely the multipath effect or (non-line-of-sight) NLOS reception [4]. The reflected signal with an extra propagation path will introduce a bias in the GNSS pseudorange measurement, which will further degrade the positioning accuracy. The GNSS degradation caused by the multipath effects that is related to the number and size of surrounding buildings, namely the urbanization of the environment, which can be quantitatively represented by the parameters of the sky-view blockage (as shown in the graphical abstract, namely skymask) [5]. The relationship between the averaged building elevation angle (or averaged skymask) and the weighted least squares positioning error from a commercial-grade GNSS

This work is supported in part by Research Institute for Sustainable Urban Development at Hong Kong Polytechnic University under the project BBWK.

G. Zhang, H. Xu and L-T. Hsu are with the Interdisciplinary Division of Aeronautical and Aviation Engineering, Hong Kong Polytechnic University, Kowloon, Hong Kong (e-mail: [guo-](mailto:guo-)

[hao.zhang@connect.polyu.hk](mailto:hao.zhang@connect.polyu.hk);

[haosheng.xu@connect.polyu.hk](mailto:haosheng.xu@connect.polyu.hk);

[lt.hsu@polyu.edu.hk](mailto:lt.hsu@polyu.edu.hk)).

P. Xu is with Hong Kong Applied Science and Technology Research Institute Company Limited, New Territories, Hong Kong (e-mail: [xphsean12@163.com](mailto:xphsean12@163.com)).

receiver is demonstrated in Fig. 1. Such positioning degradation is possible to exceed tens of meters and has become the primary issue for GNSS urban positioning.

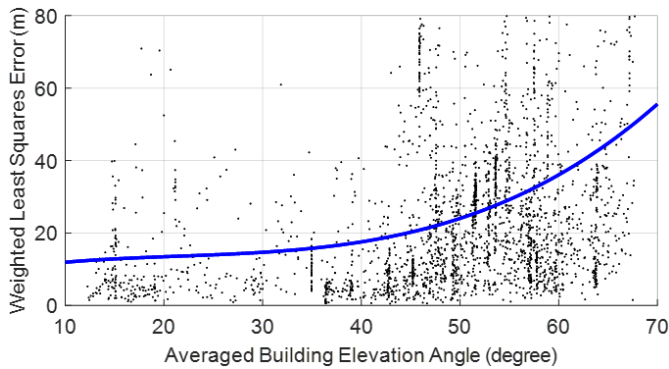


Fig. 1. Relationship between the averaged building elevation angle and the weighted least squares positioning error from a commercial-grade GNSS receiver. Blue curve denotes the polynomial fitted model from a large size of GNSS data samples (black markers).

A variety of studies have been conducted to mitigate the multipath or NLOS errors. A straight-forward method is to detect those measurements containing multipath errors by other indirect quality information (e.g., the measurement carrier-to-noise ratio  $C/N_0$ , the satellite elevation angle, etc.) and further de-weight or isolate their influences [6-9]. However, many of the multipath or NLOS errors do not follow the expected behavior, such as the strong reflection with high  $C/N_0$ , resulting in miss-detection and fault isolation. Another approach is to avoid encountering the multipath or NLOS degradation via positioning error prediction and path planning technique [10, 11], but it is impossible to avoid such errors in a dense urban area completely. Numerous studies propose employing additional sensors to compensate for the GNSS errors to achieve precise positioning solutions even in a GNSS-degraded environment, such as integrating GNSS with the inertial navigation system (INS) [12-14] and vision sensors [15, 16]. Unfortunately, the GNSS is the major sensor providing the absolute user position, which still needs to be accurate during the initialization of other sensors. Recently, a novel approach has been developed to predict the GNSS degradations via 3D building models and, in turn, employs those degradations as features to conduct positioning, namely the 3DMA GNSS. One of the popular 3DMA GNSS techniques is shadow matching [17], which conducts positioning by finding the location with the 3D-building-model-predicted satellite visibility best matching the actual measurements. Besides matching the satellite visibility, the 3DMA GNSS ray-tracing [18] further considers the matching of pseudorange delay between measurements and the 3D-building-model-based prediction. Although the 3DMA GNSS can achieve positioning accuracy with 10 meters of error in a dense urban area [19], the corresponding computation load is huge and the availability of 3D building models cannot always be guaranteed.

Due to the rapid development in computer science, it becomes possible to use computational models to learn representations of existing data, which can, in turn, guide the system behavior when a similar situation is encountered. Machine learning model is trained by adjusting the parameters

of a template model so that the input features extracted can be used to infer the outcome, which is the true label. The trained model becomes a representation between existing data features and corresponding outcomes. As a result, it can be used to predict the outcome for a new event. Various machine learning algorithms have been developed to conduct classification with satisfactory performances, such as the decision tree (DT) [20] employing a flowchart-like structure to learn and predict the outcome of an event based on existing features, or the support vector machine (SVM) [21] separating labeled feature point into groups by hyperplanes for future prediction. Moreover, the recent popular deep learning technique can even learn complicated representation from abstract raw data without the need for feature extraction guided by experts [22]. The conventional deep learning algorithm as the fully connected neural networks (FCNNs) mimics the neural structures in the human brain to solve classification or regression problems [23]. This structure is then extended by the convolution operation, namely the convolutional neural networks (CNN), to accomplish more difficult and abstract tasks, such as image recognition or diagnosis [24, 25]. By adding the artificial memory unit and forget gate into the neural network structure, such as the long short-term memory (LSTM) networks of the recurrent neural networks (RNN) [26], the model can also have an awareness of the context during prediction, which is powerful on speech recognition or translation tasks [27, 28].

The machine learning technique is superior in accomplishing tasks without expertise of the inner principles but with numerous data. For the GNSS measurement error that are complicated to be comprehensively modeled, many studies also suggest employing the machine learning technique to predict and mitigate [29]. The occurrence of GNSS ionospheric scintillation can be detected by the SVM model [30, 31] or the DT model [32] with an accuracy better than the conventional threshold-based method. The occurrence of the multipath effect in an urban area can also be detected via an SVM classifier [33]. Moreover, a machine learning random forest model can evaluate the level of multipath degradation to aid the integration of GNSS with other sensors [34]. Besides, the machine learning model can be employed in a regression manner for the pseudorange error prediction [35]. The performances of multipath detection by machine learning with different levels of GNSS measurements are investigated in [36].

Besides the conventional learning architecture, a deep learning architecture is recently being employed to extract a better representation from the GNSS data. The neural networks have been employed to better estimate the wind speed from the GNSS reflectometry (GNSS-R) measurements [37, 38]. The neural network framework is employed for multipath detection [39] or multipath error prediction [40] based on the GNSS measurement-level features, e.g., pseudorange measurements and  $C/N_0$  in the Receiver Independent Exchange (RINEX) format. It can be integrated with the fuzzy logic principle to achieve better accuracy on multipath or NLOS detection [41]. The neural network architecture can even extract representations from the GNSS correlator-level data to estimate parameters for multipath mitigation [42], or directly output the multipath-mitigated measurements [43]. This approach is further extended by integrating the CNN to conduct multipath detection and mitigation [44], or substitute the conventional

correlation process in a GNSS receiver [45]. The deep learning algorithm has shown great potential to learn and represent those complicated GNSS errors that are hard to be modeled via the traditional approach. However, most studies evaluate the benefits of GNSS aided by deep learning from the result point of view, whereas the representation that the network has learned is seldom investigated or discussed.

In this study, a deep learning framework combining conventional neural networks and LSTM is developed to predict the GNSS satellite visibility and pseudorange error in an urban canyon. Here, the satellite visibility refers to whether the satellite is blocked by buildings even if its measurement is received (i.e., NLOS reception). The pseudorange error refers to the delay within the GNSS ranging measurement due to interferences from buildings. This is inspired by our previous work that the GNSS measurements can be used to estimate the sky visibility in an urban canyon [46]. The LSTM layer is superior to FCNNs in extracting the context information from sequential data, like GNSS measurements. It is employed to extract the representation, which may relate to the environment from the preprocessed GNSS features. On the other hand, the GNSS measurement-level features of each satellite will be input to the FCNNs, from which the hidden layer will concatenate with the representation from the LSTM layer to predict the satellite visibility and pseudorange multipath error, respectively. The proposed model is trained and evaluated by real experimental data. Based on the knowledge of environment

and measurement error behavior, we conduct investigations on what representation is learned from the data and its relationship to the actual surrounding environment. The contributions of this study are twofold: 1) the development of a deep learning network architecture to predict the GNSS satellite visibility and pseudorange error in an urban area, by employing the LSTM specialized in extracting context representations; 2) the investigation on what representation is learned from the deep learning network to predict the urban GNSS measurement uncertainty (i.e., the satellite visibility and pseudorange error), and its relationship between the network layer and the urban environment.

The remainder of this paper is organized as follows: Section II shows the overall system architecture of the deep learning networks. Section III illustrates the preprocessed GNSS features that are effective for deep learning prediction. The proposed deep learning networks are explained in detail in Section IV, followed by experimental evaluation results in Section V. Then, the extracted representation from the LSTM layer is investigated in Section VI. Finally, the conclusions are summarized with future work.

## II. SYSTEM ARCHITECTURE

The proposed deep learning network architecture for GNSS satellite visibility and pseudorange error prediction is shown in Fig. 2. Firstly, the GNSS raw measurements are preprocessed to obtain the features, including the elevation angle, azimuth

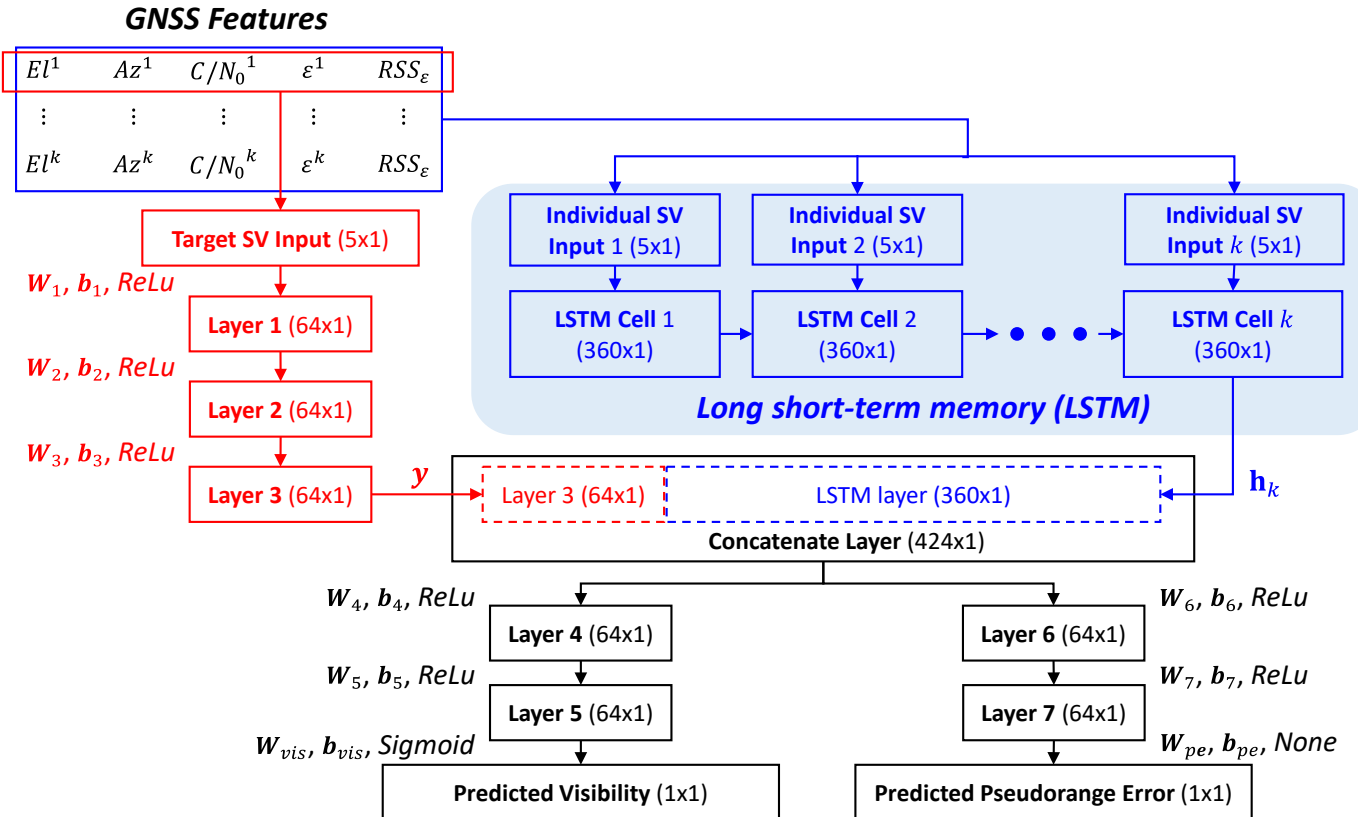


Fig. 2. The system architecture of the proposed deep learning network for satellite visibility and pseudorange error prediction. The variables  $El$ ,  $Az$ ,  $C/N_0$ ,  $\varepsilon$  and  $RSS_\varepsilon$  denote the GNSS features of elevation angle, azimuth angle, carrier-to-noise ratio, pseudorange residual, root-sum-squares of pseudorange residuals, respectively. The variable  $k$  denotes the satellite index in the same epoch of measurements.  $W$  and  $b$  denote the weighting and bias term between different neural network layers, followed by the type of activation function, including ReLU, Sigmoid and None (explained in Section IV.A). The bracket in each block denotes the size of the corresponding layer.

angle,  $C/N_0$ , pseudorange residual, and the root-sum-squares of the pseudorange residuals  $RSS_e$  from all satellites at a single epoch. In this study, the term “epoch” denotes an instant in time collecting the GNSS measurements. The GNSS features from all available satellites in a specific epoch will be the inputs of the LSTM network. This network (the blue one in Fig. 2) is expected to combine the information from each satellite to transform them into a vector that representing the surrounding environment of the GNSS receiver. The features of **a single** target satellite in the same epoch will be used as the inputs to the FCNN (the red one in Fig. 2) to predict the GNSS measurement quality in urban areas. The third hidden layer is then concatenated with the preceding layer, expecting to combine the measurement information with the environment information. The concatenate layer will be employed by two individual FCNNs with two hidden layers to predict the satellite visibility and the pseudorange error corresponding to the selected measurement. Here, the motivation of designing this network structure is to employ the LSTM’s ability in context recognition to extract a representation of the surrounding environment, which can better aid the prediction of satellite visibility and pseudorange error that is closely depending on the surrounding environment.

### III. GNSS FEATURE EXTRACTION

Although one of the benefits of deep learning is the ability to directly extract abstract representations from the raw data, the preprocess of the data can help to isolate irrelevant features and enhance the effectiveness of model training. In our proposed network, five features closely related to the satellite visibility and pseudorange error are preprocessed for the deep learning networks, including the elevation angle, azimuth angle,  $C/N_0$ , individual pseudorange residual, and the root-sum-squares of pseudorange residuals from all available satellites.

#### A. Elevation Angle $El$

The GNSS measurement quality is highly affected by the corresponding satellite elevation angle, which has been widely employed to determine the weighting during GNSS positioning. As Fig. 3a shows, the satellite with a higher elevation angle is less likely to be blocked by obstacles. Moreover, the corresponding measurement is also less affected by the multipath effect, since it is harder to fulfill the geometrical requirement of receiving the reflected signals.

The satellite elevation angle can be estimated from the GNSS measurements by

$$El = \arcsin(\hat{u}_{sv}/\hat{r}) \quad (1)$$

where  $\hat{u}_{sv}$  is the length of the “Up” component of the satellite position in East-North-Up (ENU) coordinate with respect to the receiver position,  $\hat{r}$  is the range between satellite and receiver. Although the exact positions of satellite and receiver are unknown, the elevation angle can still be estimated with an acceptable accuracy based on the ephemeris-estimated satellite position and the measurement-estimated receiver position, since positioning error is trivial compared to the distance between satellite and receiver.

#### B. Azimuth Angle $Az$

The satellite azimuth angle is another geometrical parameter describing the position of the satellite. Unlike the satellite elevation angle, it only indirectly relates to the GNSS measurement quality when considering the spatial correlations between different satellites. For a group of satellites with adjacent azimuth angles, such as Satellites 9 and 87 in Fig. 3b, if the satellite with a lower elevation angle has good measurement quality that possibly being a LOS satellite, the other satellite with a higher elevation angle is more likely to be a LOS satellite as well. On the other hand, the low-elevation satellite with an azimuth angle adjacent to a high-elevation NLOS satellite is more likely to be an NLOS satellite as well, such as Satellites 95 and 93 in Fig. 3b. Such relationships are difficult to be represented via conventional model but may be feasible by deep learning approach, which is good at extracting abstract representations.

Similar to elevation angle, the satellite azimuth angle can be estimated by the estimated satellite and receiver positions, using

$$Az = \arctan(\hat{e}_{sv}/\hat{n}_{sv}) \quad (2)$$

where  $\hat{e}_{sv}$  and  $\hat{n}_{sv}$  are the length of the “East” and “North” component of the satellite position in ENU coordinate with respect to the receiver position.

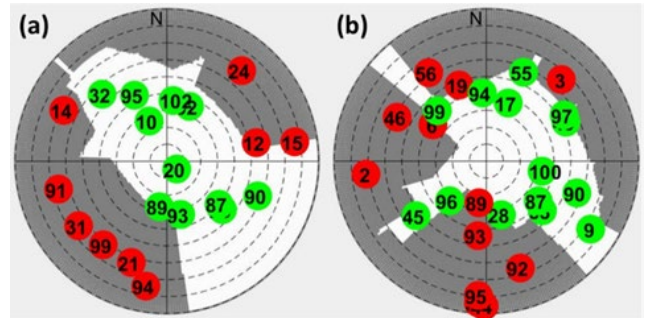


Fig. 3. Examples of the sky-plot with satellite visibility in urban areas. Green and red markers denote the LOS and NLOS satellites, respectively. Grey areas denote the sky-view blocked by buildings.

#### C. Carrier-to-Noise Ratio $C/N_0$

The quality of GNSS measurement is also frequently evaluated by its corresponding  $C/N_0$ , which describes the received signal strength with respect to the noise power density at the receiver front-end [47].

Besides being employed to determine the weighting of each measurement during positioning, the  $C/N_0$  is also used to predict satellite’s visibility in many 3DMA GNSS algorithms [17]. Moreover, the  $C/N_0$  attenuation could also relate to the interference, such as reflections or diffractions, according to the geometrical parameters of the interference [48, 49]. Therefore, the measurement  $C/N_0$  is employed to classify the satellite visibility and quantitatively evaluate the severeness of the interference. An example is shown in Fig. 4, where the measurement with severe diffraction effect is usually significantly attenuated. Noted that the  $C/N_0$  is closely related to the satellite elevation angle due to the propagation distance in space [50]. The  $C/N_0$  is a feature that usually used together with the elevation angle for an effective machine learning architecture.

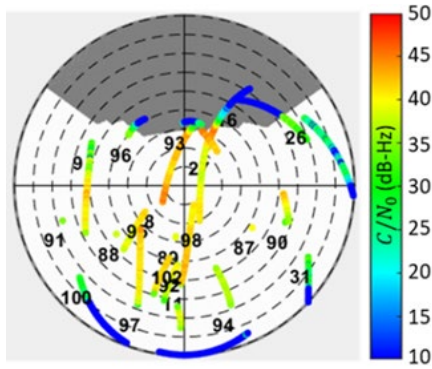


Fig. 4. A sky-plot demonstrating the  $C/N_0$  of different satellites in an urban area. The color bar shows the value of  $C/N_0$ . The grey area denotes the sky-view blocked by buildings.

#### D. Pseudorange Residual

The GNSS receiver position is usually obtained by an iterative least squares (LS) estimation based on the pseudorange measurements and satellite positions, which forms an overly determined system, as follows.

$$\Delta \mathbf{x} = (\mathbf{H}^T \mathbf{H})^{-1} \mathbf{H}^T \Delta \mathbf{p} \quad (3)$$

where  $\Delta \mathbf{x}$  consists of the position bias from the initial guess and the receiver clock bias.  $\mathbf{H}$  is the satellite geometry matrix that consisted by LOS vectors between the satellites and receiver.  $\Delta \mathbf{p}$  is the vector of the difference between pseudorange measurements and geometric distance from the initial guess to the satellites. The optimized solution may not always be consistent with all measurements. Hence, the consistency between the optimal solution and each individual measurement can be described by the pseudorange residual [9], as follows.

$$\boldsymbol{\varepsilon} = \Delta \mathbf{p} - \mathbf{H} \cdot \Delta \mathbf{x} \quad (4)$$

where  $\boldsymbol{\varepsilon} = [\varepsilon^1 \dots \varepsilon^k]^T$  consists of the individual pseudorange residual from 1<sup>st</sup> to  $k^{\text{th}}$  satellite. The pseudorange residual is expected to provide quantitative information about the scale of the pseudorange error during deep learning.

#### E. Root-Sum-Squares of Pseudorange Residuals $RSS_\varepsilon$

The goodness of the least square fit to the measurement during positioning can be evaluated by the root-sum-squares of all pseudorange residuals [51], which can be derived using

$$RSS_\varepsilon = \sqrt{\boldsymbol{\varepsilon}^T \cdot \boldsymbol{\varepsilon}} \quad (5)$$

where the superscript T denotes the transpose of a matrix. The  $RSS_\varepsilon$  can be regarded as an overall feature describing the quality of a set of GNSS measurements. It also has an indirect relationship with the environment; for example, the  $RSS_\varepsilon$  of the measurements is anticipated to be small for an open-sky area but large for an urban area. The  $RSS_\varepsilon$  is expected to provide overall information about the surrounding environment of the receiver.

## IV. DEEP LEARNING NETWORKS

As Fig. 2 shows, the proposed deep learning network combines the conventional FCNNs and the LSTM network, a popular type of RNNs. The detailed procedures and benefits of applying the proposed network will be introduced in this section.

#### A. Fully Connected Neural Networks (FCNNs)

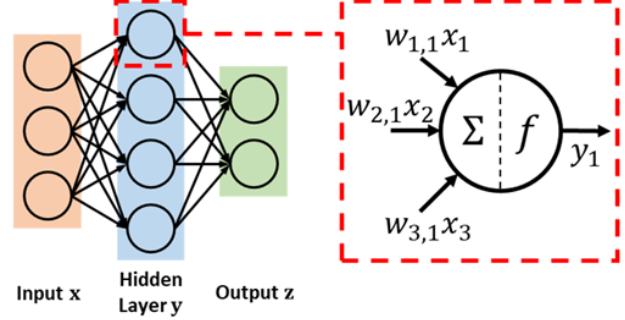


Fig. 5. Demonstration of fully connected neural networks (FCNNs) and the operation on each node.

The FCNNs architecture is a traditional form of neural networks. Each node is connected to the nodes on the next layer with all possible connections until reaching the output, as shown in Fig. 5. The mathematical process on each node can be described as applying a non-linear activation function on the biased linear combination of all the information from the former layer, as follows.

$$y_n = g(\sum_m w_{m,n} x_m + b_n) \quad (6)$$

where  $m$  and  $n$  denote the node index on the former layer and the current layer. Variable  $w_{m,n}$  denotes the weighting (coefficient) during the linear combination of each  $x_m$  from the former layer on the  $n^{\text{th}}$  node at the current layer.  $b_n$  is the bias term and  $g(\cdot)$  is the activation function. In this study, three types of activation functions may be used.

$$g(a) = \begin{cases} \max(0, a), & ReLU \\ \frac{1}{1+e^{-a}}, & Sigmoid \\ a, & None \end{cases} \quad (7)$$

The process on the whole layer can be represented in a vector form, using

$$\mathbf{y} = f(\mathbf{W}\mathbf{x} + \mathbf{b}) \quad (8)$$

Therefore, the overall network can be regarded as a repeating stack of linear combinations and non-linear functions. The goal is to find the optimal weighting and bias for each layer, making the outputs of the network (by feeding with existing data) close to the true label.

#### B. Long Short-Term Memory (LSTM) Networks

Besides using the FCNNs, our proposed network architecture employs the LSTM to obtain the representation from all available satellite information within a single epoch, as Fig. 2 shows. The motivation here is the attempt to extract the environment information, which determines the GNSS

interference behaviors, from available measurements. The feasibility of extracting this representation has been investigated by [46], where the sky-view blockage (skymask) due to buildings can be estimated by the GNSS measurements. The LSTM being widely applied on context-awareness applications is an appropriate architecture to achieve this task.

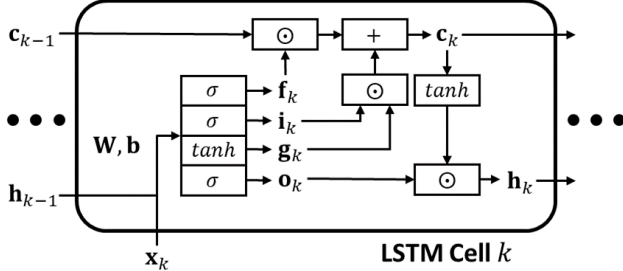


Fig. 6. Demonstration of the  $k^{\text{th}}$  cell of the long short-term memory (LSTM) architecture in the proposed network (Fig. 2).

An example cell of the employed LSTM architecture (a single LSTM layer is formed by  $k$  cells, where  $k$  is the total satellite number in a single epoch for this study) is shown in Fig. 6. Based on the current input  $\mathbf{x}_k$  and the former cell output  $\mathbf{h}_{k-1}$ , the output of the current cell can be obtained by

$$\mathbf{f}_k = \sigma(\mathbf{W}_{x,f}\mathbf{x}_k + \mathbf{W}_{h,f}\mathbf{h}_{k-1} + \mathbf{b}_f) \quad (9)$$

$$\mathbf{i}_k = \sigma(\mathbf{W}_{x,i}\mathbf{x}_k + \mathbf{W}_{h,i}\mathbf{h}_{k-1} + \mathbf{b}_i) \quad (10)$$

$$\mathbf{g}_k = \tanh(\mathbf{W}_{x,g}\mathbf{x}_k + \mathbf{W}_{h,g}\mathbf{h}_{k-1} + \mathbf{b}_g) \quad (11)$$

$$\mathbf{o}_k = \sigma(\mathbf{W}_{x,o}\mathbf{x}_k + \mathbf{W}_{h,o}\mathbf{h}_{k-1} + \mathbf{b}_o) \quad (12)$$

$$\mathbf{c}_k = \mathbf{f}_k \odot \mathbf{c}_{k-1} + \mathbf{i}_k \odot \mathbf{g}_k \quad (13)$$

$$\mathbf{h}_k = \mathbf{o}_k \odot \tanh(\mathbf{c}_k), \mathbf{h}_k \in (-1,1) \quad (14)$$

where  $\mathbf{W}$  and  $\mathbf{b}$  denote the weightings and bias that need to be trained.  $\mathbf{c}_k$  is the vector of internal recurrent cell state.  $\mathbf{f}_k$  denotes the forget gate vector determining whether to erase the cell state, whereas  $\mathbf{i}_k$  denotes the input gate vector determining whether to update the cell state.  $\mathbf{g}_k$  controls how much to update from the input, while  $\mathbf{o}_k$  controls how much to output from the cell.  $\sigma$  and  $\tanh$  are the sigmoid function and the hyperbolic tangent function, respectively.  $\odot$  denotes the element-wise multiplication.

The LSTM is capable of learning the context information shared by multiple feature sets, even for size-varying inputs [22]. It is ideal for the GNSS measurements, in which the total receivable satellite number varies depending on the environment. The design of LSTM can mitigate the extreme gradient problem on nodes during the training process via properly designed flows [25]. When dealing with a sequential input data by a traditional network architecture, the early input data has a less influence on the final network output. The LSTM mitigates this effect. However, the LSTM also has another characteristic of memorizing the input sequence pattern, which may not be an advantage for the expecting task in this study. The overall environment behavior will not have a relationship with the input sequence of measurements from different

satellites within the same epoch. To avoid over-learning the sequence pattern, we randomly rearrange the measurement order before fed in the LSTM.

### C. Training Networks

The goal of deep learning is to tune and learn the optimal parameters on each layer that can not only represent the relationships between existing feature data and the corresponding true labels, but also predict the outcome from new observations. Here, the feature data refers to the five features in Section III extracted from the received measurements of a satellite, while the true labels refer to the actual satellite visibility and pseudorange error that estimated from reliable knowledge (e.g., user's actual location and building models). During the learning process, each batch of data is fed into the networks to obtain the corresponding output. The consistency between this output and the true label is evaluated through a cost function. In this study with two outputs, the loss function is defined as an equal-weighted summation of the binary cross-entropy from the satellite visibility prediction and the mean absolute error from the pseudorange error prediction, as below.

$$\mathcal{L} = -\frac{1}{N} \sum_j^N \{y_j \log[p(y_j)] + (1 - y_j) \log[1 - p(y_j)] + |\hat{z}_j - z_j|\} \quad (15)$$

where  $j$  denotes the index of the data set (feature set of a single satellite) inside the batch data with  $N$  total size.  $y_j$  is the binary label value (1 and 0 corresponding to LOS and NLOS).  $p(y_j)$  denotes the probability of the prediction being  $y_j$  after going through the networks.  $\hat{z}_j$  and  $z_j$  denote the predicted pseudorange error from the networks and the true labeled pseudorange error, respectively.

After estimating the input gradient on each node via back-propagation from the output, a gradient descent optimization method is employed to obtain the optimal parameters that minimizing the loss function. When new GNSS measurements are received, the corresponding satellite visibility and pseudorange error can be predicted by applying the proposed network with the trained parameters.

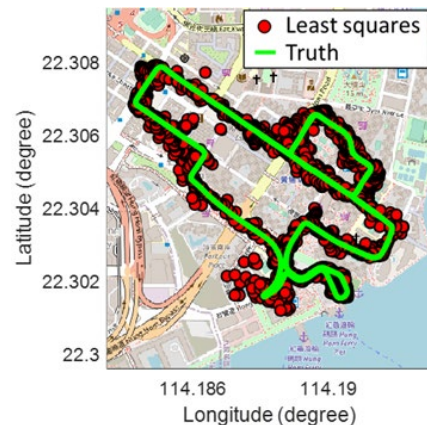


Fig. 7. The vehicular experiment trajectory for data collection. Red markers denote the least-squares positioning solution based on the collected data.

## V. EXPERIMENTAL RESULTS

### A. Experiment Setup

The performance of the proposed deep learning networks on predicting the satellite visibility and the pseudorange error is validated by real data collected from a vehicular experiment in an urban area of Hong Kong (Whampoa, 23/08/2019, at around 8 a.m. UTC), as Fig. 7 shows. The GNSS L1 measurements, including GPS and Beidou, are collected in the RINEX format based on a commercial-grade GNSS receiver ublox EVK-M8T with a standard patched antenna. The receiver true location is obtained from the real-time kinematic (RTK) GNSS/INS integrated solution from NovAtel SPAN-CPT, which is capable of achieving centimeter-level accuracy in RTK mode. The satellite visibility is labeled by comparing the satellite position with the skymask, which is obtained by remapping the 3D building model to the sky-view on the receiver's true location. The measurement with visible direct signal but under multipath effect is also categorized into LOS. The pseudorange error is labeled by extracting the building interference term via the double difference method based on the measurements and true locations of the receiver and a nearby reference station. The detail can be found at Section 2.3.3 in [36]. 3000 epochs of data are collected, where four-fifths of data are used for training, and the rest is used as the test set for out-of-sample performance evaluation. The deep learning networks are constructed and trained based on Python in TensorFlow with the application programming interface of Keras, which includes the activation functions and cost loss functions in this study.

### B. GNSS Availability Prediction Results

The satellite-wise visibility prediction result is compared with the truth labeled from the 3D building model, as shown in Fig. 8. The rapidly changing environment during a dynamic test will make the visibility classification more difficult; for example, the measurements may have a delayed reflection about the environment changing. However, the proposed deep learning networks can correctly predict the satellite visibility for most of the time, even for the satellite rapidly changing between LOS and NLOS (e.g., G02 and G29). Moreover, the proposed network has good prediction performance on all satellites, rather than only for a few particular satellites, showing a good generalization performance. Besides, the network returns a continuous value between 0 to 1 for visibility prediction instead of a binary result, which could also provide the reliability of prediction in a sense.

The final satellite visibility prediction can be determined in a binary form based on a threshold. The satellite with a visibility value over 0.5 is classified as LOS; otherwise, it is classified as NLOS. By comparing with the true visibility label, the classification performance of the proposed networks is shown in Table I. 64.0% of the total data are LOS measurements being correctly classified, and 16.2% of the total data are correctly classified into NLOS. However, there still remain 20% of the data unable to be predicted with the correct visibility information. The overall classification performance metrics of the proposed model (DL) are compared with standard support vector machine (SVM) model [33] and decision tree (DT) model in Table II, including recall, precision, F1-score, and accuracy. Here, F1-score is the harmonic mean of recall and

precision with equal importance. Noted the SVM or DT model is employed without using the feature of azimuth angle, since it cannot input multiple satellite data at once to utilize the azimuth correlations. In summary, the proposed deep learning network significantly improves the NLOS prediction performance compared to the SVM approach, achieving an overall accuracy of 80.1% for the satellite visibility prediction in the urban canyon.

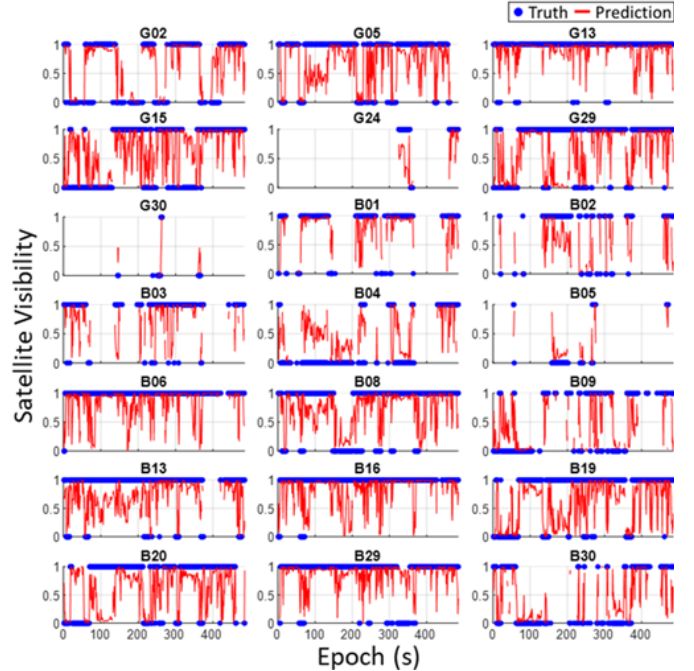


Fig. 8. The satellite visibility prediction results from the proposed deep learning network compared with the true visibility determined from the ground truth location and the 3D building model. Y-axis shows the visibility value that 1 denotes LOS and 0 denotes NLOS.

TABLE I  
SATELLITE VISIBILITY CLASSIFICATION RATE (AMOUNT OF DATA)

		Truth	
		LOS	NLOS
Prediction	LOS	64.0% (4511)	7.8% (551)
	NLOS	12.0% (849)	16.2% (1140)

TABLE II  
SATELLITE VISIBILITY CLASSIFICATION PERFORMANCE

		Recall	Precision	F1-Score	Accuracy
SVM	LOS	55.7%	74.7%	63.8%	52.0%
	NLOS	40.2%	22.2%	28.6%	
DT	LOS	76.3%	87.3%	81.5%	73.6%
	NLOS	64.9%	46.4%	54.1%	
DL	LOS	84.2%	89.1%	86.6%	80.1%
	NLOS	67.4%	57.3%	62.0%	

### C. GNSS Pseudorange Error Prediction Results

The satellite-wise pseudorange error prediction results from the proposed deep learning networks are shown in Fig. 9. Since the data is collected from a dynamic test in an urban area, the labeled pseudorange errors have a drastic variation even for the same satellite within a short period. Many of the errors exceed

20 meters, which are probably due to multipath or NLOS receptions. From the prediction results of Satellite G05 and B19, the proposed model can provide a timely prediction on the pseudorange error with a similar amplitude to the label, even if the errors may suddenly exceed 40 meters for only a few seconds. Moreover, the proposed model can instantly recognize the measurement is recovered to a healthy status, preventing over-correction. However, there still occur some epochs that the proposed model provide incorrect predictions, such as over-correction or miss-correction. Note that for the Satellites G15, B13 and B29, the proposed model cannot provide appropriate correction to those large pseudorange errors during the epochs between 150 and 200. This is probably because the receiver is under a road bridge in this period, where the environment behavior is quite different from most of the training data that only surrounded by buildings. The deep learning network is less likely to learn those representations between the measurements and pseudorange errors in the scenario under a bridge from limited training data. Therefore, the proposed model cannot provide satisfactory predictions for this scenario. In summary, for many of the time, the proposed deep learning networks can provide a timely prediction on the pseudorange error with satisfactory accuracy.

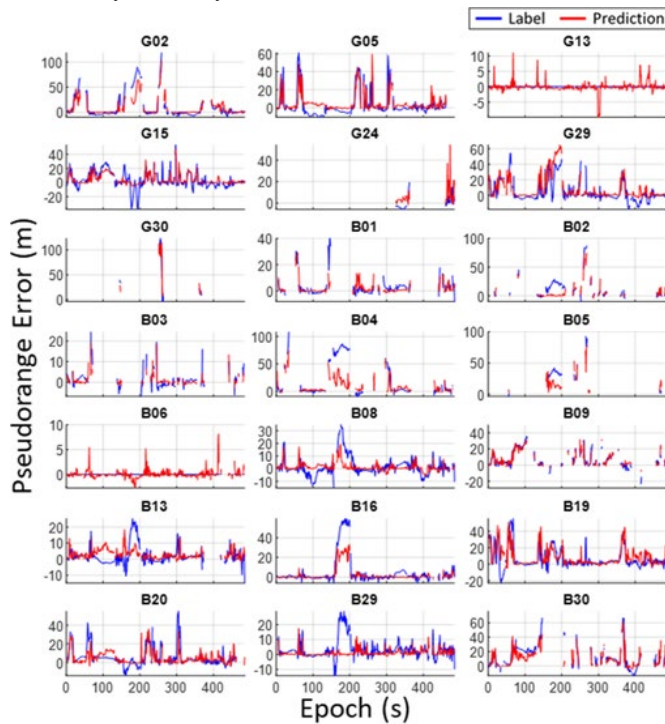


Fig. 9. The pseudorange error on each satellite based on the prediction result using the proposed deep learning network and the labeled pseudorange error from the double difference estimation.

The overall prediction results and the remained error after the correction by prediction are shown in Fig. 10. Excepting for the data from 2400 to 3000 under a bridge, most of the pseudorange errors are properly corrected, remaining only a few meters of error, which is less likely to introduce severe positioning error. The overall prediction performance is evaluated in Table III, by comparing the mean and standard deviation (STD) of the pseudorange error before and after correction from the SVM model, the DT model, or the proposed network (DL), in terms of LOS, NLOS, and all satellites. For the LOS satellites, either

receiving only the direct signal or under the multipath effect, the faulty correction from the SVM model may even degrade the pseudorange accuracy. On the other hand, the proposed deep learning networks can provide corrections that reducing the pseudorange error STD from 7.3 m to 5.3 m, which is probably profited by the corrections on the multipath error. Since the pseudorange measurements from a commercial-grade receiver may always have few meters of random thermal noise, there still remain 3.6 m errors on average after correction for the LOS satellites. For the NLOS measurements, the proposed model can mitigate half of the pseudorange error, from 18.7 m to 9.0 m on average. For the overall correction performance, the proposed network outperforms the SVM model. In a short summary, the pseudorange error can be significantly reduced in terms of mean and STD by the predictions from the proposed deep learning networks.

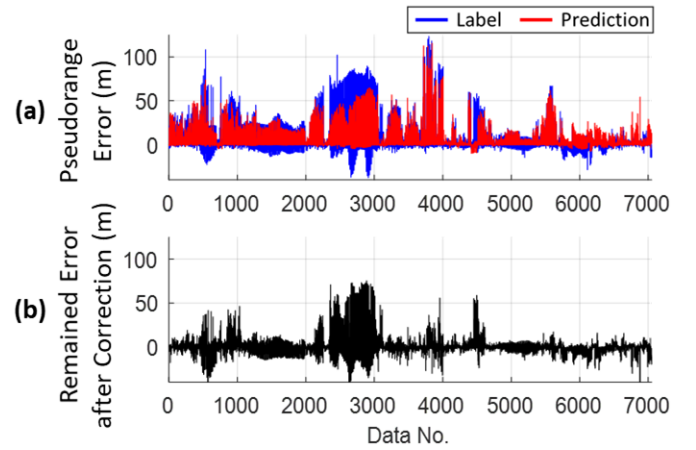


Fig. 10. (a) The labeled and predicted pseudorange errors during the dynamic experiment (test set); (b) The remained error after correcting the labeled pseudorange error by the prediction from deep learning networks. The x-axis denotes the index number of satellite-wise data.

TABLE III  
MEAN (STANDARD DEVIATION) OF PSEUDORANGE ERROR (M) FROM LOS/NLOS/ALL SATELLITES BEFORE/AFTER APPLYING THE CORRECTION PREDICTED BY THE SVM, DT, AND THE PROPOSED NETWORK (DL)

	LOS	NLOS	ALL
<b>Before</b>	3.7 (7.3)	18.7 (20.7)	7.3 (13.6)
<b>After SVM</b>	4.5 (6.2)	14.1 (16.7)	6.8 (10.6)
<b>After DT</b>	5.6 (8.2)	12.3 (14.0)	7.2 (10.3)
<b>After DL</b>	3.6 (5.3)	9.0 (12.3)	4.9 (7.9)

#### D. Deep Learning Networks Generalization Analysis

The performance of the proposed deep learning network is evaluated by two additional experiments to analyze its generalization, as Fig. 11 shows. Test A is at a similar location but different time (Whampoa, 21/05/2021, 1510 epochs at around 6 a.m. UTC) compared to the test in Section V.A, while Test B is at a different location and time (Tsim Sha Tsui, 17/05/2021, 87 epochs at around 2 a.m. UTC). The testing data here are available at [52]. The GNSS satellite visibility and pseudorange error prediction performance from the proposed network for these two experiments are summarized in Tables IV and V.

For Test A, the proposed network achieves an overall 82.0% accuracy on the satellite visibility prediction, similar to the

preceding test. The prediction on the LOS satellites is also around 20% better than that on the NLOS satellites. Consistent performance on pseudorange error prediction is achieved compared to the preceding test, where the averaged remained errors after applying correction are 9.3 m and 4.4 m for NLOS satellites and all satellites, respectively. For Test B, the visibility prediction accuracy on LOS satellites is decreased, resulting in a degradation of the overall accuracy. The GNSS measurements are severely degraded in Test B, having a doubled NLOS pseudorange error compared to the preceding test. The proposed network trained in another area still provides the pseudorange error prediction with a certain accuracy, which mitigates the pseudorange error from 17.7 m to 11.4 m on average. The degradation of prediction performance in Test B is probably because of the difference in building style. The buildings in Test B are covered by glasses, whereas the buildings in Test A and the training/validating test are covered by concrete surfaces. Hence, the GNSS measurements behave differently in these two areas and affect the prediction performance. In summary, the performance of the proposed deep learning network can be maintained for the data from different time spans. However, it will be degraded for the data from different locations, especially with a different environmental context.

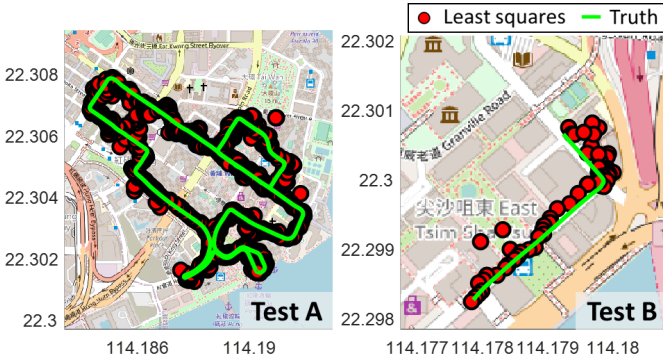


Fig. 11. The vehicular experiment trajectory for the generalization test. Test A is at the same urban area as the experiment in Section V.A, while Test B is at a different urban area. Red markers denote the least-squares positioning solution based on the collected data.

TABLE IV

SATELLITE VISIBILITY CLASSIFICATION PERFORMANCE

		Recall	Precision	F1-Score	Accuracy
Test A	LOS	87.9%	87.9%	87.9%	82.0%
	NLOS	64.9%	64.8%	64.8%	
Test B	LOS	65.9%	75.1%	70.2%	68.3%
	NLOS	71.4%	61.5%	66.1%	

TABLE V

MEAN (STANDARD DEVIATION) OF PSEUDORANGE ERROR (M) FROM LOS/NLOS/ALL SATELLITES BEFORE/AFTER APPLYING THE CORRECTION PREDICTED BY THE PROPOSED NETWORK (DL)

		LOS	NLOS	ALL
Test A	Before	2.4 (4.4)	14.9 (16.7)	5.6 (10.8)
	After DL	2.8 (4.8)	9.3 (10.6)	4.4 (7.3)
Test B	Before	3.7 (4.9)	36.2 (45.5)	17.7 (34.2)
	After DL	4.8 (4.9)	20.0 (22.7)	11.4 (17.1)

## VI. INVESTIGATION ON THE LSTM LAYER

Unlike conventional machine learning approaches, the effectiveness of a trained deep learning network is hard to be validated from the model point of view. The deep learning method truncates the modeling problem into multiple layers with a massive number of tuning parameters and nonlinear functions. It is very difficult to evaluate the goodness of each parameter or reveal the meaning of each layer. However, it is still worth investigating what has been modeled inside the deep learning networks, in order to guarantee the model is reasonable and so that it can provide a guide for future developments. For this study, both the satellite visibility and the pseudorange error are mainly affected by the environment. Therefore, for a reasonable model, it is expected to exist layers capable of extracting representations about environmental information. Therefore, in this section, we will investigate whether the LSTM layer output in our proposed networks could represent the environment information based on the test in Section V.A.

### A. Relationship between LSTM Layer and Prediction

We will first investigate whether the LSTM layer affects the prediction result in a way similar to the environment information, by manually assigning different LSTM layer vectors which is  $\mathbf{h}_k$  given in (14). In the other words, we set the value  $\mathbf{h}_k$  in the blue network (environment network) and uses the real data in the red network (measurement quality network) to investigate the performance of the prediction on the satellite visibility and pseudorange error. The six test sets of the real data are selected and they are summarized in Table VI. The corresponding sky-plots with building blockages are shown in Fig. 12. The six tests cover the typical environments in an urban canyon. The investigation steps are demonstrated in Fig. 13. The measurement features from different test sets are fed into our proposed deep learning network (Fig. 2), applying the process of FCNNs Layers from 1 to 3 (red ones). Then, the corresponding Layer 3 output will be concatenated with a manually assigned LSTM layer (blue ones), which is a 360-by-1 vector with the same entry value  $\tau$ ,  $\mathbf{h}_k = [\tau; \dots; \tau]_{360 \times 1}$ . After that, the concatenated layer (the black ones) will be processed by the remaining networks to obtain the corresponding predictions on the satellite visibility and the pseudorange error.

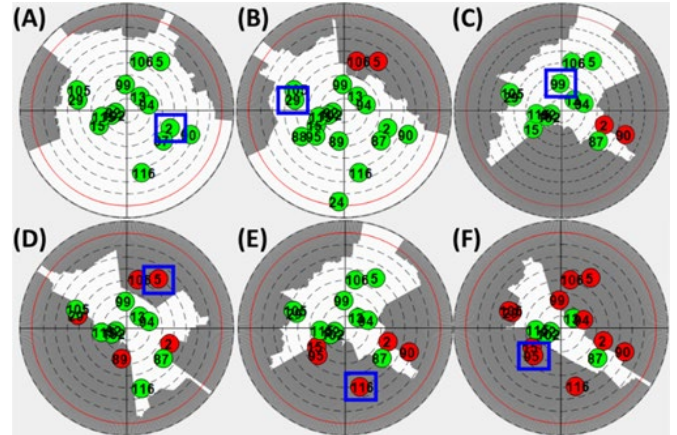


Fig. 12. The skyplot with satellites and sky-visibility for the selected data sets corresponding to Table VI by the index (A-F). Green and red markers denote LOS and NLOS satellites, respectively. Grey area denotes the sky-view blocked by buildings.

TABLE VI

INFORMATION ABOUT THE SELECTED FEATURE SETS FOR INVESTIGATION

Index	Satellite No.	Visibility	C/N <sub>0</sub> (dB-Hz)	Pseudorange Error (m)	Environment
A	2	LOS	44	0.2	Nearly open-sky
B	29	LOS	48	0.1	Barely urban
C	99	LOS	35	-0.1	Light urban
D	5	NLOS	28	22.6	Middle urban
E	116	NLOS	24	37.0	Dense urban
F	95	NLOS	24	16.6	Harsh urban

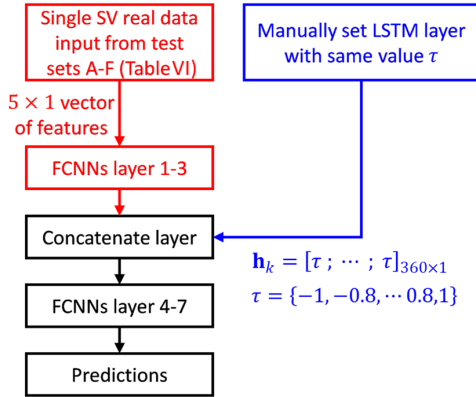


Fig. 13. The flowchart of investigating the relationship between LSTM layer and prediction result by manually assigning different  $\tau$  for the LSTM layer vector.

Based on the activation function used to calculate  $\mathbf{h}_k$ , we substitute  $\tau$  from -1 to 1. Thus, we can evaluate the relationship between the LSTM layer (blue ones) and the prediction outcome (black ones). Since the satellite visibility and pseudorange error are closely related to the surrounding environment, their prediction result would have similar behaviors regarding to different  $\tau$ .

The satellite visibility predictions on different test sets corresponding to different LSTM layer vectors are summarized in Fig. 14. Most of the predictions follow a similar behavior that the satellite is more likely to be classified as a LOS under the LSTM layer with  $\tau = \pm 1$ , but more likely to be an NLOS satellite when  $\tau = 0$ . It might indicate that a higher magnitude of  $\tau$  represents the environment closer to open-sky, where most satellites are classified into LOS. On the contrary, the LSTM layer with  $\tau = 0$  might represent a harsh urban scenario, where most of the sky-view is blocked by buildings, and most satellites are classified into NLOS. Noted for the test set B, it is still predicted as very likely being LOS even under a harsh urban scenario with  $\tau = 0$ . This is probably because its  $C/N_0$  feature is very high as 48 dB-Hz, which is strong evidence that it is LOS. In summary, the values of the LSTM layer are probably indicated to environment information, which affects the later prediction on the satellite visibility.

On the other hand, the pseudorange error prediction results for different test set with respect to different LSTM layer values are shown in Fig. 15. Similar to the preceding results on visibility prediction, the pseudorange predictions of different test sets have similar behaviors corresponding to the LSTM layer value. When giving the LSTM layer with  $\tau$  close to 0, the network is likely to predict the same level of pseudorange error

for different sets, similar to a systematic error shared by those sets. Such error is more likely to be the dominated error in an environment without other complex interference or sky-view variation. Hence, we can assume the LSTM layer with  $\tau$  close to 0 may represent an open-sky environment. Moreover, a positive pseudorange error is always predicted for a positive  $\tau$  and vice versa. A higher magnitude of  $\tau$  is also resulting in a higher variation on the error prediction. Therefore, we can assume that the positive or negative LSTM layer may represent the constructive or destructive interference (caused by the relative phase between the LOS and reflected signal) during the pseudorange error prediction. The magnitude of the layer value may represent the complexity of the environment, such as the building blockage level.

In summary, from the analysis result, the LSTM layer might represent the environment information that aiding the satellite visibility and pseudorange error prediction in the later networks.

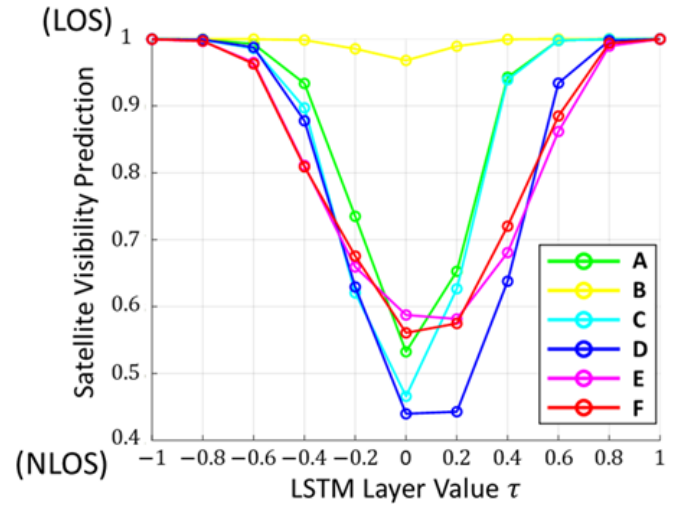


Fig. 14. The satellite visibility prediction results based on the manually assigned LSTM layer vector with the same entry  $\tau$  for different test sets from Table VI.

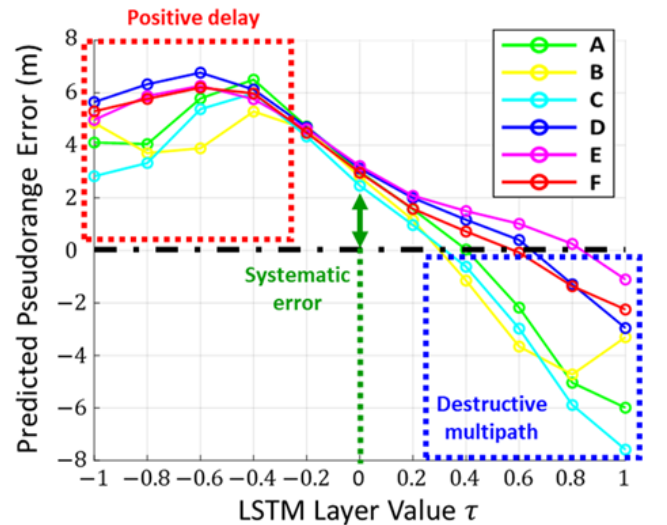


Fig. 15. The pseudorange error prediction results based on the manually assigned LSTM layer vector with the same entry  $\tau$  for different test sets from Table VI.

### B. Relationship between LSTM Layer and the Skymask

As discussed in Section VI.A, the value  $\tau$  could be associated to the environment information, e.g., the skymask. The skymask is represented by the building boundary elevation angles on each azimuth angle, which can be obtained from the receiver true location and the 3D building model. We believe the values on the LSTM layer could be associated with the values of the skymask. We intuitively assume that the value of a specific entry of the LSTM layer (an element in  $\mathbf{h}_k$ ) would be related to the skymask elevation angle on a specific azimuth angle, representing the building blockage area on that specific azimuth angle. Then, we compare the LSTM layer output with the skymask for several test sets (same as Section VI.A) to investigate the occurrence of our assumption. Instead of using 6 single satellites indicated in Table VI, we include all the satellites shown in A-F of Fig. 12. The skymasks (represents azimuth and elevation angles in x-axis and y-axis, respectively) for the test sets (indicated in Fig. 12) are shown in Fig. 16a. The grey areas in Fig. 16a indicates the azimuth angles of the existing GNSS measurements (that refers to Fig. 12). Out of the grey areas, 8 observable sections are selected to be investigated whether they can be reflected by different entries of the LSTM

layer. The environment information obtained from the skymask is summarized in Table VII for each test set and each observation section. We categorize the environment information into 5 classes (in the bracket of Table VII) based on the skymask elevation angle, which indicates the openness level of the environment on a specific azimuth direction. Based on the discovery in Section VI.A that a higher magnitude of the LSTM layer value denotes an open-sky environment, each entry of the LSTM layer from the 6 test sets (Fig. 16b) can also be categorized into 5 classes representing different levels of openness of an environment. We found 8 entries having the categorization result consistent with the openness level of preceding 8 selected observable sections for the test sets. The values of these 8 entries for different test sets and the corresponding openness level are summarized in Table VIII. Take the observable ② as an example, the skymask elevation angle on the azimuth angle of 32 degrees from A-F test sets are 14, 60, 0, 62, 0, and 78 degrees, which can be categorized into (+), (--), (++), (--), (++), and (---) to represent the environment openness level. On the other hand, the value on the 289<sup>th</sup> entry of the LSTM layer from A-F test sets are 0.67, 0.46, 0.88, 0.12, 0.93, and 0.14, which can also be categorized into (+), (-), (++),

TABLE VII

ENVIRONMENT INFORMATION (SKYMASK ELEVATION ANGLE AND THE LEVEL OF OPENNESS) ON DIFFERENT SELECTED AZIMUTH ANGLES FOR DIFFERENT TEST SETS

Observable Section Index	1	2	3	4	5	6	7	8	
Azimuth Angle (degree)	12	32	72	111	226	237	253	288	
Skymask Elevation Angle (degree)	A	28 (+)	14 (+)	32 (-)	0(++)	0(++)	0(++)	31 (-)	32 (-)
	B	60 (--)	60 (--)	49 (-)	0(++)	0(++)	0(++)	27 (+)	28 (+)
	C	0(++)	0(++)	54 (--)	50 (-)	71 (---)	14 (+)	37 (-)	45 (-)
	D	60 (--)	62 (--)	30 (-)	54 (--)	78 (---)	75 (---)	62 (--)	54 (--)
	E	0(++)	0(++)	60 (--)	50 (-)	76 (---)	70 (---)	34 (-)	45 (-)
	F	74 (---)	78 (---)	71 (---)	62 (--)	70 (---)	69 (--)	66 (--)	53 (--)

The level of the openness is categorized in 5 classes based on the elevation angle of the skymask: (++) below 10; (+) between 10-30; (-) between 30-50; (--) between 50-70; (---) over 70.

TABLE VIII

ENVIRONMENT INFORMATION REPRESENTED BY THE SPECIFIC LOCATION IN LSTM LAYER CORRESPONDING TO THE SELECTED ENVIRONMENT INDEX (FROM TABLE VII)

Observable Section Index	1	2	3	4	5	6	7	8	
LSTM Layer Entry No.	322	289	111	134	275	115	260	26	
LSTM Layer Absolute Value	A	0.30 (--)	0.67 (+)	0.69 (+)	0.81 (++)	0.25 (--)	0.64 (+)	0.54 (-)	0.45 (-)
	B	0.41 (-)	0.46 (-)	0.40 (-)	0.98 (++)	0.60 (+)	0.67 (+)	0.63 (+)	0.69 (+)
	C	0.72 (+)	0.88 (++)	0.55 (-)	0.76 (+)	0.06 (---)	0.48 (-)	0.65 (+)	0.36 (--)
	D	0.15 (---)	0.12 (---)	0.53 (-)	0.12 (---)	0.10 (---)	0.04 (---)	0.15 (---)	0.11 (---)
	E	0.97 (++)	0.93 (++)	0.31 (--)	0.35 (--)	0.02 (---)	0.19 (---)	0.57 (-)	0.54 (-)
	F	0.26 (--)	0.14 (---)	0.07 (---)	0.01 (---)	0.07 (---)	0.09 (---)	0.35 (--)	0.18 (---)

The openness level is categorized in 5 class based on the value of the selected entry from the LSTM layer: (++) over 0.8; (+) between 0.6-0.8; (-) between 0.4-0.6; (--) between 0.2-0.4; (---) below 0.2.

(---), (++) and (---) to represent the environment openness level. The representations of the openness level are quite consistent between the skymask and the LSTM layer value for each test set. Hence, the 289<sup>th</sup> entry of the LSTM layer may represent the environment information (openness level) on the 32 degrees azimuth direction during the satellite visibility prediction. Similar consistency can be found in other observable sections. Most of the categorization results between the skymask and the LSTM layer are consistent, or at least having adjacent categories. Here, the categorization rules follow an intuitive approach with equal intervals, whereas the deep learning networks could follow a non-linear model to represent the openness level. The overall trend on representing the environment openness level is quite similar between the skymask (Table VII) and the LSTM layer (Table VIII). To summarize, some parts of the LSTM layer obtained from the GNSS measurement by the proposed deep learning networks may represent the surrounding environment information.

## VII. CONCLUSIONS AND FUTURE WORKS

In this paper, we proposed a deep learning network architecture, which combines the conventional FCNNs and the popular LSTM, to predict the GNSS satellite visibility and

pseudorange error in an urban area based on the available GNSS measurements. The design of integrating the LSTM layer is aiming to learn environment representations from measurements, which determines the occurrence and severeness of the GNSS interferences in an urban area. By knowing the environment information, the deep learning networks could have a potential to provide better predictions about the GNSS interferences. The performance of the proposed deep learning network is evaluated through real experimental data. The proposed networks achieve satisfactory performance on both satellite visibility and pseudorange error predictions, which has 80.1% overall accuracy and a 4.9 m averaged difference from the labeled pseudorange error. Then, we analyze what representations have been learned by the proposed network, by investigating whether the LSTM layer extracted from the GNSS measurements contains the representations about the environment information. By comparing the LSTM layer value with the prediction outcome and the real environment information from the 3D building model, we find the LSTM layer could extract the environment representations, such as the level of openness, from the existing GNSS measurements.

This study provides a straightforward approach to investigate the representations obtained in the deep learning network.

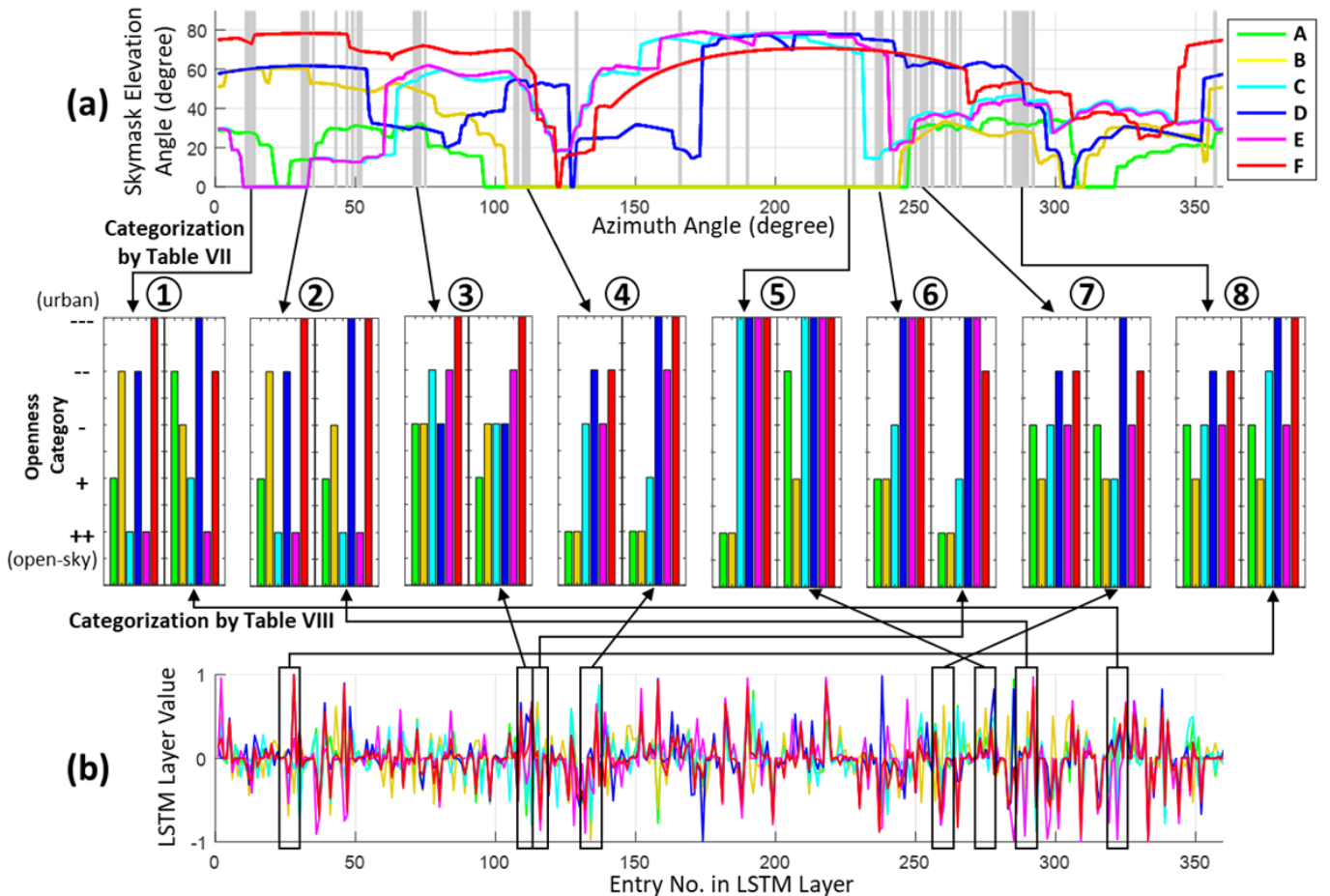


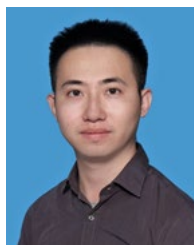
Fig. 16. The comparison between environment information represented by (a) the elevation of the building boundary on the sky-plot (skymask) according to the receiver true location and the 3D building models; (b) the value of each entry of the LSTM layer output vector (360-by-1) corresponding to different test sets. The line color denotes different test sets in Section VI.A. The number denotes the index of the selected observable section for comparison. The grey area denotes the azimuth angle with available satellite measurements, which may be the area with environment information observable by received measurements and the deep learning network.

However, the current analysis result only indirectly supports our assumptions, whereas stronger evidence is necessary for justification. To understand the representations during the deep learning network, it is suggested to analyze the meaning of each part from different hidden layers and visualize each layer based on existing knowledge. A more comprehensive and rigorous analysis of the extracted representations during the deep learning network will be conducted in the future. Moreover, the proposed deep learning network predicts the measurement status based on the data from a single epoch, whereas the transitions over the time are neglected. In addition, the receiver filtering technique will introduce a latency on the GNSS feature variation, which may degrade the prediction performance and instantaneity. The development of deep learning networks considering the historical correlations of GNSS measurement for the prediction will be a suggested future work. Exploring new GNSS features containing additional environment information will be another future work to improve the performance of the deep learning model.

## REFERENCES

- [1] F. Dovis, L. Ruotsalainen, R. Toledo-Moreo, Z. Z. M. Kassas, and V. Gikas, "Recent Advancement on the Use of Global Navigation Satellite System-Based Positioning for Intelligent Transport Systems [Guest Editorial]," *IEEE Intelligent Transportation Systems Magazine*, vol. 12, no. 3, pp. 6-9, 2020, DOI: 10.1109/MITS.2020.2994923.
- [2] N. Zhu, J. Marais, D. Bétaille, and M. Berbineau, "GNSS Position Integrity in Urban Environments: A Review of Literature," *IEEE Transactions on Intelligent Transportation Systems*, 2018.
- [3] L.-T. Hsu, "Analysis and modeling GPS NLOS effect in highly urbanized area," *GPS solutions*, vol. 22, no. 1, p. 7, 2018.
- [4] P. Groves, "Multipath vs. NLOS signals," *Inside GNSS*, vol. 8, no. 6, pp. 40-42, 2013.
- [5] W. Wen et al., "UrbanLoco: A Full Sensor Suite Dataset for Mapping and Localization in Urban Scenes," in *2020 IEEE International Conference on Robotics and Automation (ICRA)*, 2020, pp. 2310-2316.
- [6] N. Zhu, D. Bétaille, J. Marais, and M. Berbineau, "GNSS Integrity Monitoring Schemes for Terrestrial Applications in Harsh Signal Environments," *IEEE Intelligent Transportation Systems Magazine*, vol. 12, no. 3, pp. 81-91, 2020, DOI: 10.1109/MITS.2020.2994076.
- [7] S. B. Bisnath and R. B. Langley, "Pseudorange multipath mitigation by means of multipath monitoring and de-weighting," in *Proceedings of KIS*, 2001, pp. 1-9.
- [8] P. Groves and Z. Jiang, "Height aiding, C/N 0 weighting and consistency checking for GNSS NLOS and multipath mitigation in urban areas," *The Journal of Navigation*, vol. 66, no. 5, pp. 653-669, 2013.
- [9] L.-T. Hsu, H. Tokura, N. Kubo, Y. Gu, and S. Kamijo, "Multiple Faulty GNSS Measurement Exclusion Based on Consistency Check in Urban Canyons," *IEEE Sensors Journal*, vol. 17, no. 6, pp. 1909-1917, 2017.
- [10] G. Zhang and L.-T. Hsu, "A New Path Planning Algorithm Using a GNSS Localization Error Map for UAVs in an Urban Area," *Journal of Intelligent & Robotic Systems*, vol. 94, no. 1, pp. 219-235, 2019, DOI: 10.1007/s10846-018-0894-5.
- [11] A. Shetty and G. X. Gao, "Trajectory Planning Under Stochastic and Bounded Sensing Uncertainties Using Reachability Analysis," in *Proceedings of the 33rd International Technical Meeting of the Satellite Division of The Institute of Navigation (ION GNSS+ 2020)*, 2020, pp. 1637-1648.
- [12] P. D. Groves, *Principles of GNSS, inertial, and multisensor integrated navigation systems*. Artech house, 2013.
- [13] W. Jiang, Y. Li, and C. Rizos, "Optimal Data Fusion Algorithm for Navigation Using Triple Integration of PPP-GNSS, INS, and Terrestrial Ranging System," *IEEE Sensors Journal*, vol. 15, no. 10, pp. 5634-5644, 2015, DOI: 10.1109/JSEN.2015.2447015.
- [14] A. S. El-Wakeel, A. Osman, N. Zorba, H. S. Hassanein, and A. Noureldin, "Robust Positioning for Road Information Services in Challenging Environments," *IEEE Sensors Journal*, vol. 20, no. 6, pp. 3182-3195, 2020, DOI: 10.1109/JSEN.2019.2958791.
- [15] Z. Gong, R. Ying, F. Wen, J. Qian, and P. Liu, "Tightly Coupled Integration of GNSS and Vision SLAM Using 10-DoF Optimization on Manifold," *IEEE Sensors Journal*, vol. 19, no. 24, pp. 12105-12117, 2019, DOI: 10.1109/JSEN.2019.2935387.
- [16] R. Sun, Y. Yang, K. W. Chiang, T. T. Duong, K. Y. Lin, and G. J. Tsai, "Robust IMU/GPS/VO Integration for Vehicle Navigation in GNSS Degraded Urban Areas," *IEEE Sensors Journal*, vol. 20, no. 17, pp. 10110-10122, 2020, DOI: 10.1109/JSEN.2020.2989332.
- [17] L. Wang, P. D. Groves, and M. K. Ziebart, "Smartphone shadow matching for better cross-street GNSS positioning in urban environments," *The Journal of Navigation*, vol. 68, no. 3, pp. 411-433, 2015.
- [18] L.-T. Hsu, Y. Gu, and S. Kamijo, "3D building model-based pedestrian positioning method using GPS/GLONASS/QZSS and its reliability calculation," *GPS Solutions*, journal article vol. 20, no. 3, pp. 413-428, July 01 2016, DOI: 10.1007/s10291-015-0451-7.
- [19] Ng H.F., Zhang G., and H. L.T., "Robust GNSS Shadow Matching for Smartphones in Urban Canyons," *IEEE Sensors Journal*, 2021. (accepted)
- [20] S. R. Safavian and D. Landgrebe, "A survey of decision tree classifier methodology," *IEEE transactions on systems, man, and cybernetics*, vol. 21, no. 3, pp. 660-674, 1991.
- [21] W. S. Noble, "What is a support vector machine?," *Nature biotechnology*, vol. 24, no. 12, pp. 1565-1567, 2006.
- [22] Y. LeCun, Y. Bengio, and G. J. n. Hinton, "Deep learning," vol. 521, no. 7553, pp. 436-444, 2015.
- [23] S. Haykin, *Neural networks and learning machines*. United States: Pearson Education, 2009.
- [24] Y. LeCun et al., "Handwritten digit recognition with a back-propagation network," in *Proceedings of the 2nd International Conference on Neural Information Processing Systems*, 1989, pp. 396-404.
- [25] I. Goodfellow, Y. Bengio, A. Courville, and Y. Bengio, *Deep learning* (no. 2). MIT press Cambridge, 2016.
- [26] S. Hochreiter and J. Schmidhuber, "Long short-term memory," *Neural computation*, vol. 9, no. 8, pp. 1735-1780, 1997.
- [27] I. Sutskever, O. Vinyals, and Q. V. Le, "Sequence to sequence learning with neural networks," presented at the *Proceedings of the 27th International Conference on Neural Information Processing Systems - Volume 2*, Montreal, Canada, 2014.
- [28] D. Bahdanau, K. Cho, and Y. Bengio, "Neural machine translation by jointly learning to align and translate," in *International Conference on Learning Representations (ICLR 2015)*, San Diego, United States, 2015.
- [29] L.-T. Hsu, "What are the roles of artificial intelligence and machine learning in GNSS positioning?," *Inside GNSS*, 2020.
- [30] Y. Jiao, J. J. Hall, and Y. T. Morton, "Automatic equatorial GPS amplitude scintillation detection using a machine learning algorithm," *IEEE Transactions on Aerospace and Electronic Systems*, vol. 53, no. 1, pp. 405-418, 2017.
- [31] Y. Jiao, J. J. Hall, and Y. T. Morton, "Performance evaluation of an automatic GPS ionospheric phase scintillation detector using a machine-learning algorithm," *NAVIGATION, Journal of the Institute of Navigation*, vol. 64, no. 3, pp. 391-402, 2017.
- [32] N. Linty, A. Farasin, A. Favenza, and F. Dovis, "Detection of GNSS ionospheric scintillations based on machine learning decision tree," *IEEE Transactions on Aerospace and Electronic Systems*, vol. 55, no. 1, pp. 303-317, 2018.

- [33] L.-T. Hsu, "GNSS multipath detection using a machine learning approach," in *Intelligent Transportation Systems (ITSC)*, 2017 IEEE 20th International Conference on, 2017, pp. 1-6: IEEE.
- [34] G. Zhang and L.-T. Hsu, "Intelligent GNSS/INS integrated navigation system for a commercial UAV flight control system," *Aerospace Science and Technology*, vol. 80, pp. 368-380, 2018, DOI: 10.1016/j.ast.2018.07.026.
- [35] R. Sun et al., "Improving GPS Code Phase Positioning Accuracy in Urban Environments Using Machine Learning," *IEEE Internet of Things Journal*, pp. 1-1, 2020, DOI: 10.1109/JIOT.2020.3037074.
- [36] B. Xu, Q. Jia, Y. Luo, and L.-T. Hsu, "Intelligent GPS L1 LOS/Multipath/NLOS Classifiers Based on Correlator-, RINEX-and NMEA-Level Measurements," *Remote Sensing*, vol. 11, no. 16, p. 1851, 2019.
- [37] Y. Liu, I. Collett, and Y. J. Morton, "Application of Neural Network to GNSS-R Wind Speed Retrieval," *IEEE Transactions on Geoscience and Remote Sensing*, vol. 57, no. 12, pp. 9756-9766, 2019, DOI: 10.1109/TGRS.2019.2929002.
- [38] M. Asgarimehr, I. Zhelavskaya, G. Foti, S. Reich, and J. Wickert, "A GNSS-R Geophysical Model Function: Machine Learning for Wind Speed Retrievals," *IEEE Geoscience and Remote Sensing Letters*, vol. 17, no. 8, pp. 1333-1337, 2020, DOI: 10.1109/LGRS.2019.2948566.
- [39] Y. Quan, L. Lau, G. W. Roberts, X. Meng, and C. Zhang, "Convolutional neural network based multipath detection method for static and kinematic GPS high precision positioning," *Remote Sensing*, vol. 10, no. 12, p. 2052, 2018.
- [40] D. Min, M. Kim, J. Lee, and J. Lee, "Deep Neural Network Based Multipath Mitigation Method for Carrier Based Differential GNSS Systems," in *Proceedings of the ION 2019 Pacific PNT Meeting*, Honolulu, Hawaii, 2019, pp. 451-466.
- [41] R. Sun, L.-T. Hsu, D. Xue, G. Zhang, and W. Y. Ochieng, "GPS Signal Reception Classification Using Adaptive Neuro-Fuzzy Inference System," *Journal of Navigation*, vol. 72, no. 3, pp. 685-701, 2019, DOI: 10.1017/S0373463318000899.
- [42] A. A. Abdallah and Z. M. Kassas, "Deep learning-aided spatial discrimination for multipath mitigation," in *2020 IEEE/ION Position, Location and Navigation Symposium (PLANS)*, 2020, pp. 1324-1335: IEEE.
- [43] M. Orabi, J. Khalife, A. A. Abdallah, Z. M. Kassas, and S. S. Saab, "A Machine Learning Approach for GPS Code Phase Estimation in Multipath Environments," in *2020 IEEE/ION Position, Location and Navigation Symposium (PLANS)*, 2020, pp. 1224-1229: IEEE.
- [44] T. Suzuki, K. Kusama, and Y. Amano, "NLOS Multipath Detection using Convolutional Neural Network," in *Proceedings of the 33rd International Technical Meeting of the Satellite Division of the Institute of Navigation (ION GNSS+ 2020)*, 2020, pp. 2989-3000.
- [45] H. Li, P. Borhani-Darian, P. Wu, and P. Closas, "Deep Learning of GNSS Signal Correlation," in *Proceedings of the 33rd International Technical Meeting of the Satellite Division of The Institute of Navigation (ION GNSS+ 2020)*, 2020, pp. 2836-2847.
- [46] H. Xu, L.-T. Hsu, D. Lu, and B. Cai, "Sky visibility estimation based on GNSS satellite visibility: an approach of GNSS-based context awareness," *GPS Solutions*, vol. 24, no. 2, p. 59, 2020/03/16 2020, DOI: 10.1007/s10291-020-0973-5.
- [47] A. Joseph, "Measuring GNSS signal strength," *Inside GNSS*, vol. 5, no. 8, pp. 20-25, 2010.
- [48] G. Zhang, B. Xu, H.-F. Ng, and L.-T. Hsu, "GNSS RUMS: GNSS Realistic Urban Multiagent Simulator for Collaborative Positioning Research," vol. 13, no. 4, p. 544, 2021.
- [49] G. Zhang and L.-T. Hsu, "Performance Assessment of GNSS Diffraction Models in Urban Areas," *Navigation: Journal of the Institute of Navigation*, pp. 1-21, 2021, DOI: <https://doi.org/10.1002/navi.417>.
- [50] J. B.-Y. Tsui, *Fundamentals of global positioning system receivers: a software approach*. John Wiley & Sons, 2005.
- [51] T. Walter and P. Enge, "Weighted RAIM for precision approach," in *Proceedings of the 8th International Technical Meeting of the Satellite Division of The Institute of Navigation (ION GPS 1995)*, Palm Springs, CA, 1995, vol. 8, pp. 1995-2004: Institute of Navigation.
- [52] L.-T. Hsu, N. Kubo, W. Chen, Z. Liu, T. Suzuki, and J. Meguro, "UrbanNav: An Open-Sourced Multisensory Dataset for Benchmarking Positioning Algorithms Designed for Urban Areas," in *Proceedings of the 34th International Technical Meeting of the Satellite Division of The Institute of Navigation (ION GNSS+ 2021)*, St. Louis, MO, 2021.



**Guohao Zhang** (S'19) received the bachelor's degree in mechanical engineering and automation from University of Science and Technology Beijing, China, in 2015. He received the master's degree in mechanical engineering and currently pursuing the Ph.D. degree in the Hong Kong Polytechnic University. His research interests including GNSS urban localization, collaborative positioning and multi-sensor integrated navigation.



**Penghui Xu** received his bachelor's degree in mechanical engineering in 2015 in South China Agricultural University, Guangzhou, China. And in 2017 he received his Master degree in mechanical engineering in The Hong Kong Polytechnic University, Hong Kong. He is currently working in ASTRI (Hong Kong Applied Science And Technology Research Institute Company Limited) as an Engineer in the field of computer vision and machine learning.



**Haosheng Xu** received the B.Sc. in Thermal Energy and Power Engineering from Jilin University, China, in 2016 and M.Sc. at the Department of Mechanical Engineering, The Hong Kong Polytechnic University (PolyU), Hong Kong in 2019. He is studying as a PhD student at Interdisciplinary Division of Aeronautical and Aviation Engineering, PolyU. His research interests including in Context-Awareness based GNSS navigation and 3D mapping aided GNSS.



**Li-Ta Hsu** (M'15) received the B.S. and Ph.D. degrees in aeronautics and astronautics from National Cheng Kung University, Taiwan, in 2007 and 2013, respectively. He is currently an assistant professor with the Division of Aeronautical and Aviation Engineering, Hong Kong Polytechnic University, before he served as post-doctoral researcher in Institute of Industrial Science at University of Tokyo, Japan. In 2012, he was a visiting scholar in University College London, U.K. He is a technical representative in ION and an Associate Fellow of RIN. His research interests include GNSS positioning in challenging environments and localization for pedestrian, autonomous driving vehicle and unmanned aerial vehicle.